Chinese Chemical Letters 37 (2026) 111055

Contents lists available at ScienceDirect

Chinese Chemical Letters

journal homepage: www.elsevier.com/locate/cclet

A multifunctional carbon dot-based nanoplatform for antibacterial therapy: Integrating photodynamic, photothermal, and gas treatments

Mengyao Gao[a], Shan Sun[b,*], Hengwei Lin[b,*], Cheng Yang[a,*]

[a] Key Laboratory of Synthetic and Biological Colloids, Ministry of Education, School of Chemical and Material Engineering, Jiangnan University, Wuxi 214122, China

[b] International Joint Research Center for Photo-responsive Molecules and Materials, School of Chemical and Material Engineering, Jiangnan University, Wuxi 214122, China

ARTICLE INFO

Article history:
Received 20 December 2024
Revised 5 March 2025
Accepted 6 March 2025
Available online 8 March 2025

Keywords:
Carbon dot-based
Antibacterial
Photodynamic therapy
Photothermal therapy
Gas therapy

ABSTRACT

Novel antibacterial strategies such as antibacterial photodynamic therapy (aPDT) and photothermal therapy (PTT) have gained significant attention, however, relying on a single-treatment approach still faces challenges of insufficient therapeutic efficiency and the potential for drug resistance. In this study, a multimodal synergistic antibacterial nanoplatform by coupling a carbon monoxide (CO) donor (4-(3-hydroxy-4-oxo-4*H*-chromen-2-yl)benzoic acid (4-BA)) with carbon dots (CDs) is developed, referred to as CDs-CO, which integrates multiple antibacterial modes of aPDT, PTT, and gas therapy. This nanoplatform is designed for highly efficient antibacterial action with a low risk of inducing drug resistance. CDs are engineered to possess tailored functions, including deep-red light-triggered heat and singlet oxygen ($^1O_2$) production. After modification with 4-BA and exposure to 660 nm laser irradiation, CDs-CO exhibits favorable photothermal conversion efficiency ($\eta = 52.7\%$), robust $^1O_2$ generation, and $^1O_2$-activated CO release. Antibacterial experiments demonstrated the excellent sterilization effects of CDs-CO against both *Escherichia coli* (*E. coli*) and *Staphylococcus aureus* (*S. aureus*), underscoring the enhanced antibacterial efficiency of this multimodal nanoplatform. This study offers a rational approach for designing multimodal synergistic antibacterial platforms, highlighting their potential for effectively treating bacterial infections.

© 2025 Published by Elsevier B.V. on behalf of Chinese Chemical Society and Institute of Materia Medica, Chinese Academy of Medical Sciences.

Bacterial infections have become an increasingly serious global public health issue [1–4]. The discovery of antibiotics, one of the most significant breakthroughs in medical science, has saved countless lives from infectious diseases over the past century [5,6]. However, the extensive and repeated use of antibiotics has led to the emergence of antimicrobial-resistant bacterial infections, which have once again become a critical challenge [7,8]. Projections indicate that by 2050, antimicrobial resistance could result in 10 million deaths annually [9,10]. Therefore, it is urgent to develop non-antibiotic strategies to combat bacterial infections without inducing resistance.

Photo-mediated antibacterial strategies, which use various wavelengths of light to induce photochemical or photothermal changes in bacteria, have received considerable attention due to their non-invasive nature and high spatiotemporal selectivity [11–14]. Antibacterial photodynamic therapy (aPDT) and photothermal therapy (PTT) are the two most common phototherapies, they convert absorbed light into reactive oxygen species (ROS) or localized heat, which can damage key biomacromolecules such as phospholipids, enzymes, proteins, and DNA [15–18]. However, the antibacterial efficiency of these methods is often constrained by limited irradiation power density, shallow tissue penetration, and the short lifetime and restricted diffusion of ROS [19–21]. To overcome these limitations, it is crucial to combine treatments that operate on different antimicrobial mechanisms while minimizing the risk of drug resistance.

Gas therapy is an emerging antibacterial strategy that eliminates bacteria using gaseous molecules such as carbon monoxide (CO), nitric oxide, sulfur dioxide, hydrogen sulfide, and hydrogen [22,23]. Particularly, CO, an endogenous gas produced *via* heme catabolism by heme oxygenase in the human body and other biological systems, exhibits multiple beneficial functions, including anti-inflammation, anti-apoptosis, anti-proliferative, and cytoprotective effects [24–28]. To date, various CO donors have been developed, generally classified into metal-base and metal-free CO donors [29]. While metal-based CO donors have been successfully used in antibacterial and anti-tumor therapies, their metal content raises potential biosafety concerns and leaves their mechanisms of

* Corresponding authors.
E-mail addresses: sunshan@jiangnan.edu.cn (S. Sun), linhengwei@jiangnan.edu.cn (H. Lin), cyang@jiangnan.edu.cn (C. Yang).

https://doi.org/10.1016/j.cclet.2025.111055
1001-8417/© 2025 Published by Elsevier B.V. on behalf of Chinese Chemical Society and Institute of Materia Medica, Chinese Academy of Medical Sciences.

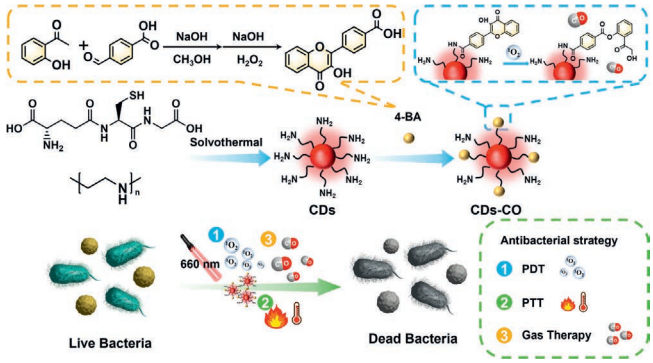


Fig. 1. Schematic illustration of the preparation of CDs-CO and their application for integrating photodynamic, photothermal, and gas treatment against bacterial infection.

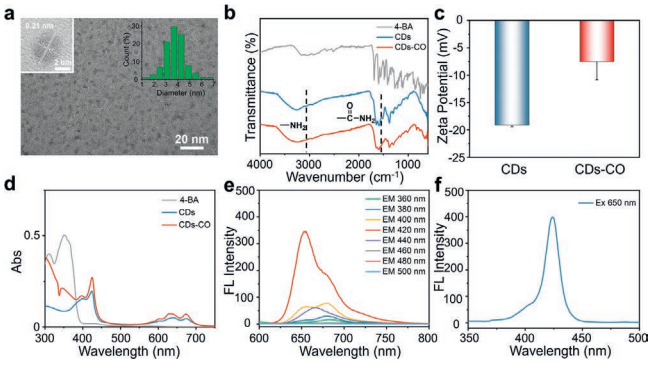


Fig. 2. (a) TEM image of CDs-CO (insert: particle size distribution and HR-TEM image). Scale bar: 20 nm (inset: 2 nm). (b) FT-IR spectra of 4-BA, CDs, and CDs-CO. (c) Zeta potentials of CDs and CDs-CO. (d) UV–vis spectra of 4-BA, CDs, and CDs-CO. (e) FL emission spectra of CDs-CO under different excitation wavelengths. (f) The FL excitation spectrum of CDs-CO.

action uncertain [30,31]. In addition, most metal-free CO donors are activated by ultraviolet (UV) light, which poses challenges due to poor tissue penetration and the risk of skin damage [32]. The development of non-metal CO donors, such as 3-hydroxyflavone (3-HF) and its derivatives, addresses these concerns and supports the construction of multifunctional antibacterial platforms.

Carbon dots (CDs), a novel zero-dimensional carbon-based nanomaterial, exhibit significant advantages in biomedical applications due to exceptional biocompatibility, low toxicity, unique optical properties, and facile surface functionalization [33–37]. Notably, the high efficiency of photo-mediated ROS and heat generation in disrupting bacterial structures make CDs as promising candidates for antibacterial therapies [38,39]. In this study, we successfully developed a multimodal antibacterial nanoplatform by modifying metal-free CO donors on dual-functional carbon dots (referred to as CDs-CO). This nanoplatform offers several key advantages: (i) The CDs are designed to possess both photothermal and photodynamic antibacterial properties, eliminating the need for additional components and simplifying the preparation process. (ii) The CO donor, 4-(3-hydroxy-4-oxo-4*H*-chromen-2-yl)benzoic acid (4-BA), is synthesized with active carboxyl groups and combined with CDs *via* an amide bonding reaction. Upon laser irradiation, the generated ROS from CDs trigger controlled CO release. (iii) Antibacterial experiments further demonstrated that CDs-CO, integrating three antibacterial mechanisms, showed superior sterilization effects against both Gram-positive and Gram-negative bacteria. Additionally, the combination of multiple antibacterial modes helps prevent the development of drug resistance. These advantages position CDs-CO as a promising platform for effective bacteria inactivation through multiple antibacterial modes of aPDT, PTT, and gas therapy.

The prepared process of CDs-CO is illustrated in Fig. 1. Initially, dual-functional CDs with both PDT and PTT properties were synthesized *via* solvothermal reaction, following the procedures established in our previous work [40]. The CO donor, 4-BA, a derivative of 3-HF, was synthesized through Claisen-Schmidt condensation and Algar-Flynn-Oyamada reaction. Detailed synthesis routes and corresponding characterizations are provided in the Experimental Section and Figs. S1–S3 (Supporting information). CDs-CO were prepared by a facile amide condensation reaction between CDs and 4-BA. The mass ratio of 4-BA in CDs-CO was determined to be 0.47 % using the amine titration method (Figs. S4 and S5 in Supporting information). The morphological structure of CDs-CO was characterized using transmission electron microscopy (TEM) and high-resolution TEM (HR-TEM). As shown in Fig. 2a, CDs-CO are shown to be well-dispersed, monodisperse spherical particles with an average diameter of approximately 3.7 nm, and a lattice spacing of 0.21 nm, corresponding to the (100) spacing plane of graphitic carbon [41]. As illustrated in Figs. S6a and b (Supporting information), the TEM and HR-TEM images reveal that the morphology of CDs closely resembles that of CDs-CO. Nevertheless, the particle size of CDs is slightly smaller at around 2.35 nm due to the introduction of 4-BA (Fig. S6c in Supporting information). Fourier transform infrared spectroscopy (FT-IR) was conducted to determine the successful bonding of CDs and 4-BA. Compared with CDs, the FTIR spectrum of CDs-CO shows an additional shoulder peak at about 1550 cm^{-1} attributed to the N–H bending vibration of the amide bond and a decreased peak at about 3060 cm^{-1} ascribed to N–H stretching vibration of amino, demonstrating the successful integration of CDs and 4-BA (Fig. 2b) [42]. The X-ray photoelectron spectroscopy (XPS) analysis of CDs and CDs-CO has been subsequently conducted. As shown in Figs. S7 and S8 (Supporting information), the XPS spectra of both CDs and CDs-CO exhibit characteristic peaks for C (284.8 eV), N (399.8 eV), O (531.8 eV), and S (163.1 eV). High-resolution XPS spectra of C 1s, N 1s, O 1s, and S 2p further confirm the presence of chemical bonds, such as C=O, C–O/C–O–C, N–C=O, C–N, and thiolate groups. Additionally, the zeta potential of CDs was measured to be -19.1 ± 0.3 mV, which positively shifted to -7.54 ± 3.3 mV after grafting with 4-BA (Fig. 2c). To further investigate the optical properties of CDs-CO, ultraviolet-visible (UV–vis) spectroscopy and fluorescence (FL) emission/excitation spectra were measured. As shown in Fig. 2d, the UV–vis absorption spectra of both CDs and CDs-CO exhibit similar absorption behavior, with characteristic bands extending into the deep-red light region, indicating their potential for deep-red light-triggered antibacterial therapy. Additionally, a new absorption peak at 350 nm was observed in the CDs-CO spectrum, which is attributed to the incorporation of 4-BA. As depicted in Fig. 2e, CDs-CO displays excitation-dependent FL emission, with the excitation wavelengths ranging from 360 nm to 440 nm. The optimal excitation wavelength of CDs-CO is at 420 nm, with the maximum emission peak at 650 nm (Fig. 2f). Furthermore, the FL emission spectra and excitation spectra of CDs were measured and found to be similar to those of CDs-CO, indicating minor effects on the optical properties of CDs after 4-BA modification (Fig. S9 in Supporting information). Finally, the colloidal stability of CDs-CO under physiological conditions was evaluated by dispersing the material in saline. As shown in Fig. S10 (Supporting information), CDs-CO exhibited excellent dispersion with no evident aggregation observed after 7 days, which is promising for biomedical applications.

To evaluate the feasibility of CDs-CO as a photothermal antibacterial agent, their photothermal properties were thoroughly studied. The photothermal conversion capabilities of CDs and CDs-CO under 660 nm laser irradiation were monitored using a ther-

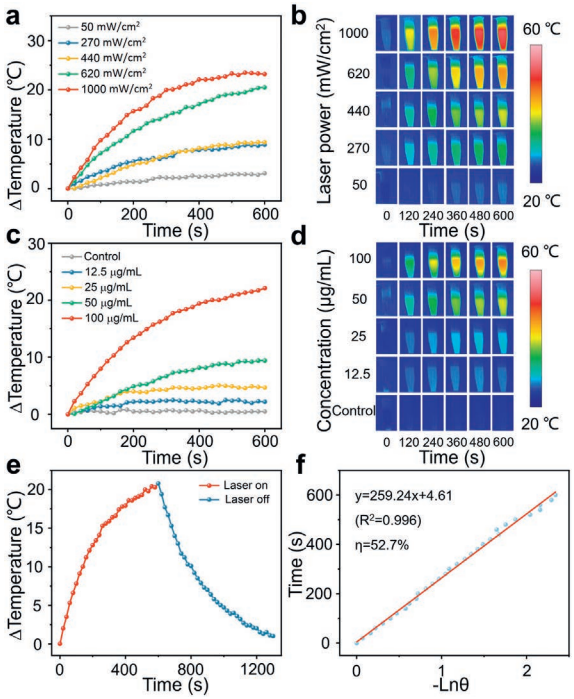


Fig. 3. (a) Photothermal heating curves and (b) real-time infrared thermal images of CDs-CO (50 μg/mL) under 660 nm laser irradiation at different power densities. (c) Photothermal heating curves and (d) real-time infrared thermal images of CDs-CO at different concentrations under 660 nm laser irradiation (440 mW/cm^2, 10 min). (e) The photothermal effect of CDs-CO (50 μg/mL) under 660 nm laser irradiation (440 mW/cm^2) for 10 min. (f) The plot of cooling time data *versus* $-\ln\theta$ and corresponding linear fitting curve.

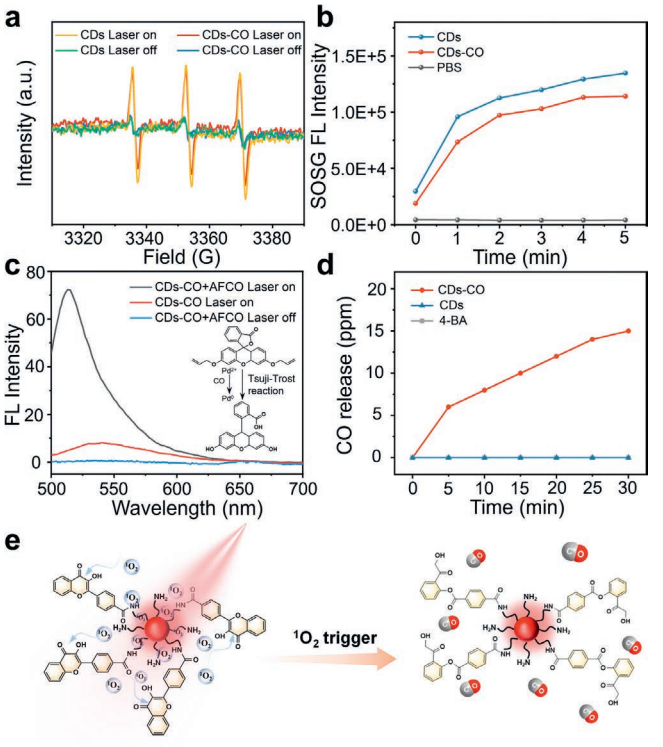


Fig. 4. (a) ESR spectra of TEMP + CDs and TEMP + CDs-CO without or with 660 nm laser irradiation (440 mW/cm^2). (b) FL intensity of SOSG at 525 nm in the presence of CDs, CDs-CO with 660 nm irradiation (440 mW/cm^2). (c) FL emission spectra of AFCO probe (10 μmol/L) and palladium chloride ($PdCl_2$, 10 μmol/L) in the presence of CDs-CO dispersion with or without 660 nm laser irradiation. (d) The CO release of 4-BA, CDs, and CDs-CO under 660 nm irradiation (440 mW/cm^2). (e) Schematic illustration of deep-red light-triggered CO release of CDs-CO.

mal imager. The photothermal properties of CDs-CO were initially assessed under varying laser powder densities. As shown in Figs. 3a and b, the temperature increase of the CDs-CO solution was positively correlated with the laser power density. The maximum temperature rise of the CDs-CO solution (50 μg/mL) reached 23 °C under 660 nm irradiation for 10 min at a power density of 1 W/cm^2. Subsequently, the laser-triggered temperature changes of CDs-CO aqueous dispersion at varying concentrations were investigated. As revealed in Figs. 3c and d, under certain laser irradiation (440 mW/cm^2, 10 min), the photothermal effect of CDs-CO was positively correlated with its concentration, while the control group showed no significant temperature change. This demonstrates that CDs-CO efficiently converts the absorbed 660 nm laser energy into heat. Moreover, the photothermal conversion efficiency (η) of CDs-CO was determined from the photothermal cooling curves shown in Fig. 3e, with the η calculated to be 52.7 % (Fig. 3f). The photothermal performance of CDs was also analyzed (Fig. S11 in Supporting information), confirming that the photothermal characteristics of CDs-CO were successfully inherited from CDs.

CDs-CO was specifically designed to harness both photothermal and photodynamic antibacterial properties. After confirming its favorable photothermal effect, the photo-induced ROS generation capacity was subsequently examined. Electron spin resonance (ESR) spectroscopy was carried out to detect the generation of ROS from CDs using 2,2,6,6-tetra-methylpiperidine (TEMP) as a trapping agent. As shown in Fig. 4a, characteristic singlet oxygen ($^1O_2$) signals were observed in both CDs and CDs-CO after 660 nm laser irradiation. In contrast, no significant $^1O_2$ ESR signals were detected in either CDs or CDs-CO without laser irradiation. These findings confirm that $^1O_2$ can be generated by CDs under 660 nm laser irradiation. The photosensitization properties of CDs-CO were further evaluated using singlet oxygen sensor green (SOSG) as the fluorescent probe in phosphate buffer saline (PBS) buffer (pH 7.4). As shown in Fig. 4b, the FL intensity of SOSG increased progressively upon laser irradiation in both CDs and CDs-CO samples. Weaker FL emission from SOSG was observed in the CDs-CO dispersion compared to that of CDs at the same concentration, indicating that 4-BA consumes a portion of $^1O_2$ to release CO. After validating the superior PTT and PDT performance of CDs-CO, the ROS-triggered CO generation was examined. The allyl-Flu (AFCO) probe, a commercial probe for CO detection, was used to monitor CO production from CDs-CO under 660 nm laser irradiation [43]. The response mechanism of the AFCO involves the reduction of Pd^{2+} to Pd^0 by CO, followed by Pd^0-mediated Tsuji-Trost reaction to remove the allyl group. As shown in Fig. 4c, strong FL signals were observed after laser irradiation of CDs-CO, confirming CO release, whereas no CO was detected from CDs-CO without irradiation. Moreover, the CO release process was monitored by a portable CO detector (Dräger Pac6500), revealing no CO production from 4-BA under laser irradiation, while significant CO release was detected from CDs-CO upon irradiation, supporting the proposed CO release mechanism (Fig. 4d). Additionally, CO release stability was investigated after a 7-day incubation in saline. As illustrated in Fig. S12 (Supporting information), comparative FL intensity between aged samples and freshly prepared aqueous dispersions (Fig. 4c) was recorded, confirming sustained photosensitivity and CO release capability in physiological conditions over extended durations. Taken together, these results demonstrate that the $^1O_2$ generated by CDs is partially utilized to oxidize 4-BA, leading to the release of CO under 660 nm laser irradiation (Fig. 4e).

Encouraged by the promising PDT and PTT performance, as well as the CO generation of CDs-CO under 660 nm laser irradiation, the antibacterial activity of the nanoplatform was further eval-

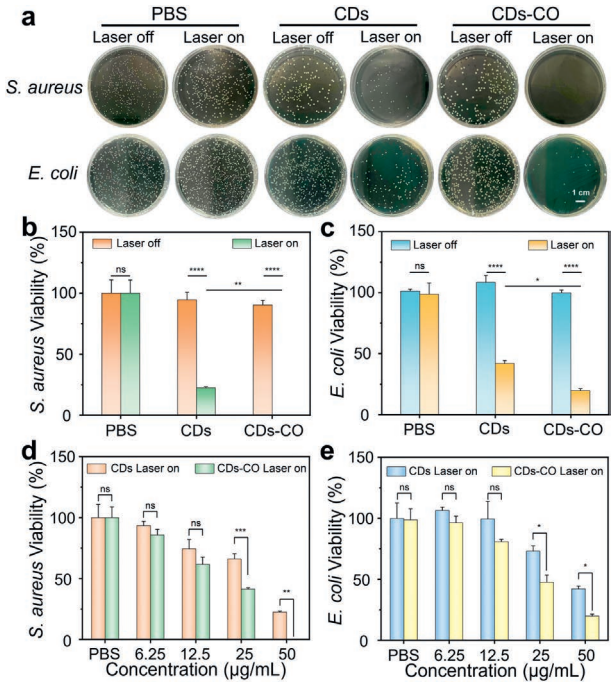


Fig. 5. (a) Agar plate digital photographs of *S. aureus* and *E. coli* after being treated with PBS, CDs, and CDs-CO (50 μg/mL) with or without laser irradiation, and corresponding survival rates for (b) *S. aureus*, and (c) *E. coli*. Scale bar: 1 cm. The relative survival rates of (d) *S. aureus*, and (e) *E. coli* treated with CDs and CDs-CO (0–50 μg/mL) under 660 nm laser irradiation (440 mW/cm^2, 20 min). $^*P < 0.05$, $^{**}P < 0.01$, $^{***}P < 0.001$, $^{****}P < 0.0001$, ns represents no significant difference. Data represent mean ± SD from three times independent experiments.

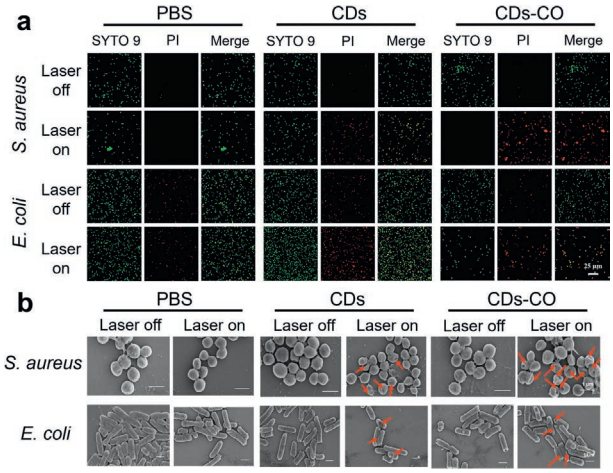


Fig. 6. (a) Live/dead FL staining images of *S. aureus* and *E. coli* after treatment with PBS, CDs, and CDs-CO with or without laser irradiation. Scale bar: 25 μm. (b) SEM images of *S. aureus* and *E. coli* after treatment with PBS, CDs, and CDs-CO with or without laser irradiation. Scale bar: 1 μm.

uated. Prior to evaluating its antibacterial efficacy, the cytotoxicity of CDs-CO was assessed by cell counting kit-8 (CCK-8) assay. 3T3 cells were co-cultured with CDs and CDs-CO, respectively, and no significant cytotoxicity was observed at a series of concentrations from 0 to 100 μg/mL, confirming the low cytotoxicity of both CDs and CDs-CO under experimental dosages (Fig. S13 in Supporting information). To directly assess the bacterial internalization ability of CDs and CDs-CO, confocal laser scanning microscope (CLSM) imaging was conducted. *Escherichia coli* (*E. coli*) was selected as the representative bacterium and incubated with CDs and CDs-CO for 30 min, respectively. Utilizing their intrinsic FL, strong red FL signals were localized within bacterial cells (Fig. S14 in Supporting information), confirming successful cellular uptake despite their negative surface charge. To evaluate the antibacterial performance, two representative strains commonly associated with wound infections, the Gram-positive *Staphylococcus aureus* (*S. aureus*) and the Gram-negative *E. coli* were selected. The antibacterial efficacy of CDs and CDs-CO, with and without laser irradiation, was evaluated using the plate colony counting method. As illustrated in Fig. 5a, both *S. aureus* and *E. coli* showed a marked reduction in colony count following laser irradiation with CDs and CDs-CO, compared to those without irradiation. Minimal viable bacteria remained after treatment with CDs-CO under laser irradiation. The corresponding quantitative results are presented in Figs. 5b and c. Additionally, the dose-dependent antibacterial activity of CDs and CDs-CO against *S. aureus* and *E. coli* was systematically analyzed. As shown in Figs. 5d and e, both CDs and CDs-CO demonstrated a dose-dependent antibacterial efficacy, with nearly 99% of *S. aureus* and 80% of *E. coli* being eliminated at a concentration of 50 μg/mL of CDs-CO under laser irradiation. Notably, both CDs and CDs-CO exhibited stronger antibacterial activity against *S. aureus* compared to *E. coli*. This observed difference is likely due to the outer membrane of gram-negative *E. coli*, which is tightly packed with lipopolysaccharides (LPS), making it more resistant to ROS compared to gram-positive bacteria like *S. aureus* [44]. Additionally, CDs and CDs-CO were ineffective in killing bacteria without laser irradiation (Fig. S15 in Supporting information), verifying their photo-mediated sterilization effect against *S. aureus* and *E. coli* bacteria. To elucidate the dominant mechanism underlying the multimodal antibacterial nanoplatform, comparative analysis of PTT, aPDT, and gas therapy modalities was conducted. Building upon prior quantitative characterization of gas therapeutic efficacy (Figs. 5b–e), the phototherapeutic modes were decoupled using L-ascorbic acid (a selective $^1O_2$ scavenger) to isolate the photothermal effect of CDs-CO (Fig. S16 in Supporting information). Quantitative plate counting revealed bactericidal rates of 13.0% (PTT), 59.2% (aPDT), and 27.8% (gas therapy). These results confirm that aPDT drives the primary antibacterial activity in our nanoplatform.

For more direct observation, Live/dead staining assays for *S. aureus* and *E. coli* were conducted and monitored by CLSM. STYO9 and propidium iodide (PI) FL dyes were employed to label all (green) and dead bacteria (red), respectively. As shown in Fig. 6a, the PBS group and non-irradiated groups exhibited minimal red FL, indicating negligible bacteria death. In contrast, significant red FL was observed in the CDs-CO group under laser irradiation, demonstrating the superior antibacterial efficiency of CDs-CO. Moreover, compared to CDs, the CDs-CO group exhibited stronger red FL, indicating enhanced antibacterial activity attributable to the incorporation of gas therapy. To further investigate the interaction of CDs and CDs-CO with *S. aureus* and *E. coli*, scanning microscopy (SEM) was carried out to observe the morphology and membrane integrity of bacteria. As depicted in Fig. 6b, bacteria in the control group and those treated with CDs or CDs-CO without laser irradiation displayed intact membranes and smooth surfaces. In contrast, bacteria exposed to laser-irradiated CDs or CDs-CO showed wrinkled and roughened surfaces. Notably, more pronounced morphological deformation was observed in bacteria treated with CDs-CO compared to those treated with CDs, indicating the exceptional antibacterial efficacy of CDs-CO. Overall, these results demonstrated that CDs-CO exhibit broad-spectrum antibacterial activity by inducing bacterial membrane damage through multiple mechanisms.

In summary, we have successfully developed a novel multimodal antibacterial nanoplatform, CDs-CO, by seamlessly integrating aPDT, PTT, and gas therapy. This nanoplatform was fabricated through the facile conjugation of CO donor (4-BA) onto the well-designed CDs. Notably, the CDs-CO exhibit high η (52.7%), abun-

dant $^1O_2$ production, and $^1O_2$-driven CO release when exposed to 660 nm laser irradiation. *In vitro* antibacterial assays revealed that the CDs-CO nanoplatform was highly effective against both *E. coli* and *S. aureus* bacteria. This study addresses the limitations of single-mode antibacterial therapies and provides a novel approach for designing multimodal antibacterial platforms.

Declaration of competing interest

The authors declare that they have no known competing financial interests or personal relationships that could have appeared to influence the work reported in this paper.

CRediT authorship contribution statement

Mengyao Gao: Writing – original draft, Methodology, Investigation, Data curation. **Shan Sun:** Writing – review & editing, Formal analysis. **Hengwei Lin:** Conceptualization. **Cheng Yang:** Methodology, Funding acquisition.

Acknowledgments

This work was supported by the National Natural Science Foundation of China (No. 52173126), and China Postdoctoral Science Foundation (No. 2024M751152).

Supplementary materials

Supplementary material associated with this article can be found, in the online version, at doi:10.1016/j.cclet.2025.111055.

References

[1] R.E. Hancock, A. Nijnik, D.J. Philpott, Nat. Rev. Microbiol. 10 (2012) 243–254.
[2] K.S. Ikuta, L.R. Swetschinski, G.R. Aguilar, et al., Lancet 400 (2022) 2221–2248.
[3] Y. Weng, H. Chen, X. Chen, et al., Nat. Commun. 13 (2022) 4712.
[4] Z. Chen, Z. Wang, J. Ren, et al., Accounts Chem. Res. 51 (2018) 789–799.
[5] N.Q. Balaban, S. Helaine, K. Lewis, et al., Nat. Rev. Microbiol. 17 (2019) 441–448.
[6] Q. Yu, C. Wang, X. Zhang, et al., ACS Nano 18 (2024) 14085–14122.
[7] X. He, Z. Xu, H. Wu, et al., Adv. Funct. Mater. 34 (2024) 2404708.
[8] P. Yuan, X. Ding, Y.Y. Yang, et al., Adv. Healthc. Mater. 7 (2018) 1701392.
[9] C.J. Murray, K.S. Ikuta, F. Sharara, et al., Lancet 399 (2022) 629–655.
[10] C. He, P. Feng, M. Hao, et al., Adv. Funct. Mater. 34 (2024) 2402588.
[11] J. Li, H. Shen, H. Zhou, et al., Mater. Sci. Eng. R 152 (2023) 100712.
[12] J. Ouyang, A. Xie, J. Zhou, et al., Chem. Soc. Rev. 51 (2022) 4996–5041.
[13] M.M. Lee, W. Xu, L. Zheng, et al., Biomaterials 230 (2020) 119582.
[14] H. Zhang, C. He, L. Shen, et al., Chin. Chem. Lett. 34 (2023) 108160.
[15] Q. Jia, Q. Song, P. Li, et al., Adv. Healthc. Mater. 8 (2019) 1900608.
[16] V. Almeida-Marrero, E. van de Winckel, E. Anaya-Plaza, et al., Chem. Soc. Rev. 47 (2018) 7369–7400.
[17] Q. Jia, J. Ge, W. Liu, et al., Adv. Mater. 30 (2018) 1706090.
[18] H. Xin, Y. Liu, Y. Xiao, et al., Adv. Funct. Mater. 34 (2024) 2402607.
[19] J. Huo, Q. Jia, H. Huang, et al., Chem. Soc. Rev. 50 (2021) 8762–8789.
[20] Y. Du, J. Zhou, F. He, et al., Nano Today 52 (2023) 101963.
[21] Y. Zhong, X.T. Zheng, S. Zhao, et al., ACS Nano 16 (2022) 19840–19872.
[22] L. Yu, P. Hu, Y. Chen, Adv. Mater. 30 (2018) 1801964.
[23] T.Y. Wang, X.Y. Zhu, F.G. Wu, Bioact. Mater. 23 (2023) 129–155.
[24] J. Cheng, B. Zheng, S. Cheng, et al., Chem. Sci. 11 (2020) 4499–4507.
[25] S.B. Wang, C. Zhang, Z.X. Chen, et al., ACS Nano 13 (2019) 5523–5532.
[26] H.I. Choi, A. Zeb, M.S. Kim, et al., J. Control. Release 350 (2022) 652–667.
[27] J. Yang, S. Pan, S. Gao, et al., Biomaterials 271 (2021) 120721.
[28] X. Ning, X. Zhu, Y. Wang, et al., Bioact. Mater. 37 (2024) 30–50.
[29] J. Cheng, J. Hu, ChemMedChem 16 (2021) 3628–3634.
[30] J. Cheng, G. Gan, Z. Shen, et al., Angew. Chem. Int. Ed. 133 (2021) 13625–13632.
[31] J. Hu, Y. Fang, X. Huang, et al., Adv. Drug Deliv. Rev. 179 (2021) 114005.
[32] L. Gao, J. Cheng, Z. Shen, et al., Angew. Chem. Int. Ed. 61 (2022) e202112782.
[33] P. Li, L. Sun, S. Xue, et al., SmartMat 3 (2022) 226–248.
[34] J. Du, N. Xu, J. Fan, et al., Small 15 (2019) 1805087.
[35] W.B. Zhao, K.K. Liu, Y. Wang, et al., Adv. Healthc. Mater. 12 (2023) 2300324.
[36] Z. Yang, T. Xu, H. Li, et al., Chem. Rev. 123 (2023) 11047–11136.
[37] Y. Xiao, X. Yin, P. Sun, et al., Chin. Chem. Lett. 33 (2022) 5051–5055.
[38] J. Wang, Y. Fu, Z. Gu, et al., Small 20 (2024) 2303773.
[39] K. Cheng, H. Wang, S. Sun, et al., Small 19 (2023) 2207868.
[40] C. Zhao, S. Sun, S. Li, et al., ACS Appl. Mater. Interfaces 14 (2022) 10142–10153.
[41] Z. Song, Y. Shang, Q. Lou, et al., Adv. Mater. 35 (2023) 2207970.
[42] S. Sun, Q. Chen, Z. Tang, et al., Angew. Chem. 132 (2020) 21227–21234.
[43] S. Feng, D. Liu, W. Feng, et al., Anal. Chem. 89 (2017) 3754–3760.
[44] W. Zhou, L. Chen, H. Li, et al., ACS Nano 18 (2024) 19771–19782.